

# Optimal fault resolution in geodetic inversion of coseismic data

Simone Atzori<sup>1</sup> and Andrea Antonioli<sup>1</sup>

<sup>1</sup> *Istituto Nazionale di Geofisica e Vulcanologia, Sezione di Roma, Italy*

## SUMMARY

With the continued growth in availability of DInSAR and GPS data, space based geodesy has been widely applied to image the coseismic displacement field and to retrieve the static dislocation over the fault plane for almost all the significant earthquakes of the past two decades. This is performed by linear data inversion over a set of subfaults, generally characterized by a constant and predefined or manually adjusted dimensions.

In this paper we propose a new algorithm to automatically retrieve an optimized fault subdivision in the linear inversion of coseismic geodetic data. The code iteratively keeps the parameter resolution close to a predefined high value. We first discuss the rationale supporting our algorithm and, after a detailed description of its implementation, we analyze the advantages of its introduction in the data inversion.

The algorithm was tested against an exhaustive range of synthetic and real datasets and fault mechanisms. Among them, we present the results for the  $M_w$  6.2, 2009 L'Aquila (Central Italy) earthquake and compare the new and previously published slip distributions showing the disappearance of misleading slip pattern and the increased resolution for shallower zones.

## 1. INTRODUCTION

Differential Interferometry from Synthetic Aperture Radar (DInSAR) is a widely used space based technique that allows the retrieval of surface displacement by comparing radar echoes

captured at different epochs (*Gabriel et al., 1989, Franceschetti and Lanari, 1999*). DInSAR maps cover wide areas with centimetric accuracy in displacement measurements, though only along the Line of Sight (LoS), i.e. the ground-satellite direction.

Thanks to the ERS (European Remote Sensing) satellite archives, starting in 1992, together with recently launched satellites (ENVISAT in 2002, ALOS in 2006, Radarsat 2 in 2007, TerraSAR-X in 2007, Cosmo SkyMed constellation from 2007), images acquired with different geometries, radar wavelengths and pixel resolutions are now available for most of the inshore earthquakes. At the same time, large permanent and temporary GPS networks have been developed in seismogenic areas providing highly accurate, 3D measurements of displacement that are often used together with DInSAR data to image the coseismic displacement fields (*Massonnet et al., 1993*).

These data are usually analyzed to retrieve the earthquake source with both non-linear and linear inversions, allowing the definition of the fault geometries and the relative slip distribution over a set of patches with a predetermined fixed dimension (*Johnson et al., 2001; Wright et al., 2003, Funning et al., 2005, Sudhaus and Jonnson, 2008, Atzori et al. 2009*).

However, this type of fault subdivision does not account for the actual slip detail that can be resolved from data: patches located at depth or in areas that are sparsely covered by measurements are often poorly constrained and only weighted averages of their slip values can be estimated (*Menke, 1989*), while other parts of the fault could be further refined.

*Page et al. (2009)* showed that an overestimation of the system resolution (i.e. imposing patches that are excessively small with respect to their ability to resolve fault details) can introduce spurious artefacts that might be improperly interpreted as asperities. *Wright et al. (2003)* provided another reason to avoid the adoption of a regular fault subdivision, highlighting how a more refined image of the slip in fault planes could also increase the accuracy in the computation of coseismic stress redistribution.

In this work we propose an iterative algorithm to subdivide the main fault into patches of variable dimensions with the constraint of keeping the resolution as close as possible to a

predefined value. The algorithm is based on the model resolution matrix and is presented with a complete description of its implementation and performance, together with example showing its application to the  $M_w$  6.2, 2009, L'Aquila earthquake (Central Italy).

## 2. PREVIOUS WORK

The idea of analyzing the resolution that can be obtained in the linear inversion of geodetic data is certainly not new and different approaches have been presented.

Many papers illustrate slip distributions supported by an analysis of the relative resolution either by means of checkerboard test or calculating model resolution matrix (*Sagiya and Thatcher, 1999; Reilinger et al., 2000, Wright et al., 2003; Funning et al., 2005; Biggs et al., 2006; Cheloni et al., 2010*, and many others). The final fault subdivision, however, is not self adaptive and in most cases the subfault patches are still uniform.

In some approaches the analysis of the resolution is followed by an adjustment of the patch size: in *Pritchard et al., (2002)*, the slip distribution retrieved for the 1995 Antofagasta (Chile) earthquake is calculated for a fault subdivision manually modified to keep the model resolution values above 0.8. In recent work on the 2004 Parkfield earthquake, *Page et al. (2009)* exploit a checkerboard test to manually redefine the patch size, increasing shallower areas at the expense of the deepest parts; an approach which is also adopted in the work of *Custodio et al. (2009)*.

*Fialko et al. (2005)* present a slip distribution for the 2003 Bam (Iran) earthquake with a fault subdivided into patches of variable size; however the adopted algorithm seems to account only for the loss of sensitivity with depth and no resolution matrix is shown.

In an empirical approach to the problem, *Lohman and Simons (2005)* adapt the fault model of *Simons et al. (2002)* for the 1999 Hector Mine earthquake, where the patch size accounts only for the depth, with the aim of keeping the model resolution matrix qualitatively more diagonal. In *Lohman and Simons (2005)* this model is used to downsample the DInSAR maps to maintain the data (rather than the model) resolution matrix close to the identity matrix.

In this paper we present a new and completely automated algorithm which provides an optimised fault subdivision that achieves the best resolution possible for the entire data set, accounting for all the factors that can affect the resolution: patch depth, data coverage, measure uncertainty and model suitability. The algorithm is easy to implement and the results are unambiguous. The algorithm is described in full and is being made freely available to the scientific community.

### 3. DESCRIPTION OF THE ALGORITHM

The algorithm is based on the model resolution matrix and aims to find the highest resolution for a given geodetic dataset. Regardless of the way the Green's function matrix  $\mathbf{G}$  is built (this aspect will be discussed in section 5), the linear relation between the data  $\mathbf{d}$  and the model parameter  $\mathbf{m}$  is described by

$$\mathbf{d} = \mathbf{G} \cdot \mathbf{m} \quad [1]$$

through which we define the model resolution matrix

$$\mathbf{R} = \mathbf{G}^{\#} \cdot \mathbf{G} \quad [2]$$

where  $\mathbf{G}^{\#}$  is the generalized inverse of the Green's function matrix  $\mathbf{G}$ . Every row in  $\mathbf{R}$  corresponds to a model parameter  $m_i$  and the values in the row describe how well the  $i$ -th parameter is solved by data: when the only nonzero value is 1 on the diagonal, the corresponding parameter  $m_i$  is perfectly solved, otherwise the data can solve only a weighted combination of parameters (*Menke, 1989*).

When  $\mathbf{R}=\mathbf{I}$  all the model parameters are perfectly solved by the data, but this condition is not sufficient to achieve the best resolution, intended as the maximum level of detail that we can have on the fault: the latter condition is obtained when, at the same time, the number of patches is maximized.

The starting configuration of the algorithm is  $\mathbf{R}=\mathbf{I}$  and can easily be obtained with a very low number of patches, at most only one. The algorithm then iteratively evolves splitting the fault, always keeping  $\mathbf{R}$  close to  $\mathbf{I}$ .

To define a convergence criterion, we set a threshold for the resolution value ( $res\_max$ ) and consider the  $i$ -th patch resolved and fixed as soon as its resolution  $res_i$  decreases just under  $res\_max$ . We set this threshold to 0.99, a parameter that can be modified in the code. We apply a second constraint based on the maximum number of patches allowed, in the case the user wants to keep the total number of patches low for computational reasons.

The algorithm iterations continue until either all the patches  $m_i$  have a resolution  $res_i$  below  $res\_max$  or the number of patches reaches the maximum permitted. In the latter case, even if the algorithm is forced to stop, the actual patch configuration is still the best achievable with the chosen parameters and can be used in the inversion.

Each iteration is divided in two steps:

#### ***Calculation of the resolution matrix***

This step only implies the calculation of the generalized inverse  $\mathbf{G}^{-g}$  of [1]. Via the Singular Value Decomposition technique (*Penrose*, 1955) we can write:

$$\mathbf{G}^{-g} = \mathbf{V} \mathbf{\Lambda}^{-1} \mathbf{U}^T \quad [3]$$

where  $\mathbf{U}$  is the eigenvector matrix spanning the data space,  $\mathbf{V}$  is the eigenvector matrix of the model space,  $\mathbf{\Lambda}$  is the matrix with the singular values  $\lambda$  on the diagonal.

Real data are always affected by errors, and singular values gradually tend to zero preventing a sharp distinction between the zero and nonzero values. To avoid the inclusion of excessively small singular values, we apply a damping factor  $\varepsilon$  and replace every singular value  $\lambda$  by  $\lambda + \varepsilon^2$  (*Menke*, 1989). We verified that the simple cut off of the singular values below an arbitrary small threshold degrades the performance of the algorithm.

There is no way other than trial and error to define  $\varepsilon$  (*Menke*, 1989); this factor regulates the trade-off between the data fit and the solution length, and as a general rule is found with an external cycle between two boundary values of  $\varepsilon$ .

Merging equations [2] and [3] we calculate the resolution matrix via

$$\mathbf{R} = \left\{ \mathbf{V} \mathbf{\Lambda}_d^{-1} \mathbf{U}^T \right\} \left\{ \mathbf{U} \mathbf{\Lambda}_d \mathbf{V}^T \right\} \quad [4]$$

where  $\mathbf{\Lambda}_d$  is the damped version of  $\mathbf{\Lambda}$ .

After the calculation of  $\mathbf{R}$ , the algorithm separates the patches into two groups: a group  $\mathbf{S}$  of perfectly solved patches, whose diagonal value  $res_i$  is greater than  $res\_max$ , and a group with the patches already below  $res\_max$ . Patches from this second group are fixed from this point forward because further subdivision would lower their resolution. Group  $\mathbf{S}$ , containing those patches that are perfectly solved by data, proceeds to the second step in the iteration where further subdivision is possible.

### ***Selection of the patches for the division***

There is a likelihood that this step will result in an over-split configuration. It can be verified that even if the patches of  $\mathbf{S}$  are split only into two parts, in a few iterations the resolution values will dramatically break down to weak values and this effect is amplified if the subdivision is carried out with more sub-patches. This occurs because the resolution of a patch is also lowered by the subdivision of the adjacent ones.

At each step we therefore select a subset of  $\mathbf{S}$  for splitting and the definition of such subset is accomplished by ordering the patches with their area  $A(i)$ , and applying three penalizing coefficients. These account for the depth of the patch ( $C_1$ ), the data coverage ( $C_2$ ) and the presence of adjacent patches already below  $res\_max$  ( $C_3$ ):

-  $C_1(i)$  has values in the range  $[0,1]$  and accounts for the decrease in resolution with depth; it is calculated as follows:

$$C_1(i) = e^{-\frac{d_i k_d}{D}} \quad [5]$$

where  $d_i$  is the patch depth,  $D$  is the base of the fault and  $k_d$  is an empirical parameter driving the priority in the patch splitting: the highest is  $k_d$ , the more penalized are the deepest patches. Even if this tuning parameter is strongly related to the fault geometry and the data coverage, reasonable values for  $k_d$  are between 3 and 5, as shown in the following section (Fig. 3b);

- the penalizing coefficient  $C_2(i)$  is in the range  $[0,1]$ , it accounts for the data coverage and is calculated as follows:

$$C_2(i) = \frac{\text{MIN}\{dist_i\}}{dist_i} \quad [6]$$

where  $dist_i$  is the planimetric distance between the  $i$ -th patch center and the closest observed point;  $\text{MIN}\{.\}$  is the minimum value of all the  $dist_i$ ;

- a third coefficient  $C_3(i)$  is applied to penalize patches surrounded by areas where the resolution limit was already reached; this coefficient is calculated as follows:

$$C_3(i) = \frac{\sum_{j=1}^M dist_{i,j} \cdot res_j}{\sum_{j=1}^M dist_{i,j}} \quad [7]$$

where  $dist_{i,j}$  is the distance between the  $i$ -th and the  $j$ -th patch and  $res_j$  is the patch resolution.

After the coefficient calculation, the patches of  $\mathbf{S}$  are sorted with decreasing values of

$$A(i) \cdot C_1(i) \cdot C_2(i) \cdot C_3(i) \quad [8]$$

where  $A(i)$  is the area of the  $i$ -th patch.

After sorting the patches in  $\mathbf{S}$ , only a percentage  $\alpha \in [0,1]$  of the area covered by the subset of  $\mathbf{S}$  is subdivided. Good values for  $\alpha$  are between 0.1 and 0.3, as shown in the next section (Fig. 3a).

The division is performed horizontally when the patch width is greater than length, vertically in the opposite case, in order to keep the aspect ratio close to 1.

Both parameters  $k_d$  and  $\alpha$  can be set for each fault geometry and data distribution, even if standard values can be used for a large number of cases, as shown in the next section.

#### 4. ALGORITHM SETTING AND PERFORMANCE

In this section we describe the algorithm settings and performance assuming perfect data and a perfect model. Under this assumption the Green's function matrix  $\mathbf{G}$  depends on the fault geometry and the data coverage only, and the final fault subdivision represents a theoretical upper limit. A

more realistic case using data with full variance/covariance matrix can be included in the definition of  $\mathbf{G}$  and is discussed in section 5. Regardless of whether we are dealing with a theoretical or realistic  $\mathbf{G}$ , the algorithm finds the optimum configuration that maintains the resolution matrix  $\mathbf{R}$  close to  $\mathbf{I}$ .

In this section we test the algorithm with different fault mechanisms and the following data coverages:

- a network of GPS stations (Fig. 1a);
- a regularly sampled DInSAR dataset (Fig. 1b);
- a DInSAR dataset sampled with a gradient based algorithm (Fig. 1c);
- a regularly sampled DInSAR dataset that partially covers the fault area (Fig. 1d).

The first two datasets are the GPS and the Envisat descending interferogram used in the modelling of L'Aquila earthquake in *Atzori et al. (2009)*; the third dataset derives from the same interferogram subsampled with the Quadtree algorithm of *Jónnson et al. (2002)*. The last dataset reproduces a displacement pattern that is only partially on land; this represents DInSAR data coverage in a typical megathrust subduction zone. For every dataset we test three different fault mechanisms: a low angle thrust fault (dip  $20^\circ$ , rake  $90^\circ$ ), a normal fault (dip  $60^\circ$ , rake  $-90^\circ$ ) and a left lateral transcurrent fault (dip  $90^\circ$ , rake  $0^\circ$ ). The surface projections of these faults with respect the data coverage are also shown in Fig. 1.

In Fig. 2 we show the preliminary resolution values of an evenly divided fault with three fault mechanisms and the dataset (a) and (b) of Fig. 1. As expected, only a small part of the fault is well-resolved (green patches); others are still too large and could be sub-divided further (yellow patches) or are too small (red patches) because in depth or sparsely illuminated by data.

The ideal solution should have green patches everywhere and in order to provide a quantitative way to describe the result, we use a Quality Index (QI in the figures) that is simply the mean value of the resolution calculated only for the patches that already are below the *res\_max* (i.e. the non-yellow patches in the Figs 2-4).

In the algorithm only two parameters need to be set,  $k_d$  and  $\alpha$  (see section 3), and they play an important role in keeping the resolution as high as possible. In Fig. 3 we show the influence of these parameters on the Quality Index (QI) for several fault geometries (see the figure caption for details). The highest QI can be obtained with  $\alpha$  below 0.4 and  $k_d$  between 3 and 5, for almost all the geometries; default values of 0.3 for  $\alpha$  and 3.5 for  $k_d$  produced good solutions for almost all the synthetic and real tests we performed. However, optimal values of the parameters are problem dependent and *ad hoc* values can be considered, if needed.

In fig. 4 we represent the performance of the algorithm showing the resolution values obtained for the data distribution of Fig. 1 applied to the fault geometries of Fig. 2. The improvement is evident and it is confirmed by the increased QI, even if some isolated patches still have a relatively low resolution value, due to the subsequent splitting of the nearby patches: this effect is marginal and tends to disappear when the data variance is included and a damped solution is required.

## 5. MODEL RESOLUTION AND DATA UNCERTAINTY

The assumption of perfect data and model sets a limit for the achievable resolution for a given case: building the Green's function matrix only on the base of data coverage and fault geometry defines the theoretical smallest patch that data can resolve at any point of the fault. Smaller patches would necessarily need some additional *a priori* smoothing and could introduce spurious artifacts (Page *et al.*, 2009).

Real data, however, are always affected by spatially correlated errors, especially DInSAR data (Hannsen, 2001; Lohman and Simons, 2005 and therein references), and these disturbances degrade the resolution that can be obtained (Menke, 1989). Such uncertainty can be accounted for by including the data variance and covariance in the computation of the Green's functions. Several papers address the subject of calculating and accounting for a full variance/covariance matrix for DInSAR data (Hannsen, 2001; Funning *et al.*, 2005; Sudhaus and Jonsson, 2008 and references therein). Similarly, the SINEX format for GPS data (Blewitt *et al.*, 1994) can come with a complete

variance/covariance matrix of the measurements. When the variance/covariance matrix is available, the linear relation [1] between the data,  $\mathbf{d}$ , and the model parameter,  $\mathbf{m}$ , is modified into

$$\mathbf{G}^T \mathbf{W} \cdot \mathbf{d} = (\mathbf{G}^T \mathbf{W} \mathbf{G}) \cdot \mathbf{m} \quad [9]$$

where the weighting matrix  $\mathbf{W}$  contains the reciprocal values of the variance/covariance matrix. This equation can be compacted in the form

$$\tilde{\mathbf{d}} = \tilde{\mathbf{G}} \cdot \mathbf{m} \quad [10]$$

where  $\tilde{\mathbf{G}}$  is the modified Green's function matrix to be given as input to the splitting algorithm. The introduction of data uncertainty in the linear system [9] imposes the damping of the singular values, as described in section 3. We remember that the damping factor  $\varepsilon$  can be chosen by trial and error (*Menke, 1989*), and this is generally performed with a cycle over the  $\varepsilon$  value: while the damping factor  $\varepsilon$  increases, the solution length (or model roughness) decreases at the expense of the data fit. Because the presented algorithm imposes the maximization of the model resolution matrix  $\mathbf{R}$ , the patch dimensions are re-determined at every value of  $\varepsilon$ . We note that the stronger the data variance, the greater is the required damping and this implies the growth of the patch size (variable across the fault). There is a perfect balance between the fault subdivision and the damping factor, while the algorithm constantly maintains  $\mathbf{R}$  close to  $\mathbf{I}$ .

Although the fault subdivision we get at every value of  $\varepsilon$  is optimized in terms of the resolution matrix, the only reliable subdivisions are the ones characterized by a realistic (i.e. not fluctuating) slip distribution and this solution is usually identifiable in the curve data fit vs. roughness. This aspect will be further clarified in the test case in section 6..

A last remark concerns the model adopted in the inversion. Although the elastic solutions of *Okada (1985)* for an homogeneous and isotropic elastic half-space are widely used in coseismic modeling, any other more realistic model for which equation [1] holds can be used to build the Green's function matrix  $\mathbf{G}$ , e.g. the elastic solution for a layered half-space (*Wang et al., 2003, Fukahata and Matsu'ura, 2005*) or the Finite Element approach described in *Trasatti et al. (2007)*.

## 6. THE 2009 L'AQUILA EARTHQUAKE

As test case we choose the 6th of April 2009,  $M_w=6.2$  L'Aquila (Central Italy) earthquake. The event had a deep social impact, both in terms of casualties (about 300) and in terms of its effects on the historical city of L'Aquila and surrounding medieval villages. Detailed description of the event can be found in, among others, *Atzori et al. (2009)*, *Chiarabba et al. (2009)* and *Cirella et al. (2009)*. The mainshock has been located at  $45.35^\circ\text{N}$ ,  $13.38^\circ\text{E}$  with a depth of 9.5 km (UTC 1:32). It was preceded by a long sequence lasting several months and culminating with an event of magnitude 4 a few days before the mainshock. This was followed by several  $M_w>5$  mainshocks and a few thousand smaller events (Fig. 5). The large number of seismic stations already installed in the region was incremented immediately after the mainshock with several temporary stations. This dense network allowed an accurate location of the events during the seismic sequence that lasted until late 2009. *Chiarabba et al. (2009)* relocated the entire sequence, clearly identifying the mainshock fault plane and the location of the main slip asperities.

The L'Aquila event is the best documented Italian earthquake in terms of space-based geodetic data: a dense GPS network, also increased a few days before the mainshock (*Anzidei et al. 2009*), and DInSAR maps from ENVISAT (C-band, ascending and descending), COSMO-SkyMed (X-band, ascending) and ALOS (L-band, ascending) satellites were available for modeling. Details of these images can be found in *Stramondo et al. (2011)*.

With the availability of the relocated aftershocks from *Chiarabba et al. (2009)* we redefined the dip of the Paganica-S. Demetrio fault ( $50^\circ$ ) and calculated a new rake angle ( $-100^\circ$ ) with a non-linear inversion. We then jointly inverted all five geodetic datasets with the proposed algorithm, from which we show the data fit vs. roughness curve (Fig. 6) for increasing values of the damping factor  $\varepsilon$ . For each value of  $\varepsilon$  the algorithm re-calculates the patch subdivision: the number of patches decreases but the QI always remains high (well above 0.9) because the algorithm keeps  $\mathbf{R}$  close to  $\mathbf{I}$ .

In this inversion, the weighting matrix  $\mathbf{W}$  of equation [9] is derived from the full variance-covariance matrix obtained from L-, X- and C-band differential interferograms, on the same area, containing only atmospheric noise. The covariance matrix for the GPS data was provided by the geodesy group of the INGV of Rome (Anzidei *et al.*, 2009).

We identify the best solution from the trade-off curve between data fit and roughness (Fig. 6), corresponding to  $\varepsilon_{best} = 0.085$ . For  $\varepsilon < \varepsilon_{best}$  the fit is slightly better, but the solution has unrealistic fluctuations; for  $\varepsilon > \varepsilon_{best}$  the smoothing is excessive and the data fit rapidly starts degrading.

In Fig. 7 we show the slip distribution corresponding to three levels of damping. Data uncertainty calls for a higher level of damping, which results into a loss of resolution on the fault (Menke, 1989).

On the left side of Fig. 7d we show the result from a linear inversion with a fault divided in patches of 1 km x 1 km, as in Atzori *et al.* (2009). The corresponding resolution values, on the right of Fig. 7d, emphasize the overestimation of the resolution power at depth and its underestimation on the surface, with only a thin strip of patches well-resolved. The comparison between the adaptive splitting and the equal sized patches shows that some fault asperities in Fig. 7d are blended into patches of larger dimensions in Fig 7b. This does not necessarily imply that the solution in Fig. 7d is wrong, but only that the resolution obtainable with the data is not sufficient to determine such a level of detail. Some asperities in the fault model represent a mathematical solution coming from the chosen patch dimension of 1 km and the required regularization. On the other hand, there is an improvement in the resolution for shallower patches that can be perfectly solved by data with dimensions much lower than 1 km (the smallest in Fig 7b is 0.28 km x 0.19 km): with an even fault division we were possibly losing such a level of detail in the upper part of faults. Though this difference in the two models would not have a strong effect on the seismic hazard of the L'Aquila event, we think that the application of the proposed algorithm gives an important added value to the determination of the coseismic dislocation for earthquakes studied with geodetic data.

A last remark concerns the data fit: in both cases (constant or variable patch size) the rms of the residuals between observed and the modelled data is substantially the same, even if the one with variable patches is slightly better (Fig. 7). This is not surprising given that the solutions of linear inversions are non-unique. The small improvement is due to the possibility of better reproducing the high frequencies of the ground displacement with the reduced dimensions of the shallower patches.

## 7. CONCLUSIONS

In this work we have presented a new algorithm for uneven fault subdivision in the linear inversion of coseismic geodetic data. The goal of the algorithm is to obtain maximum model resolution for a given data set when inverting for the distributed coseismic slip. We have described in detail the rationale, implementation and performance of the algorithm using both theoretical and real data; we analyzed the achievable resolution limit with perfect data and the decay in resolution when data uncertainty is accounted for. The role played by the “tuning” parameters is described and the default values, valid for almost all fault configurations, are provided.

The adoption of this algorithm allows the optimization of the information achievable by geodetic data in imaging slip distribution. Though the solution is intrinsically non-unique, the use of patches of equal dimension is likely to produce solutions that are mathematically correct, but somehow misleading because they could introduce spurious artifacts or are lacking in short wavelength details. The existence of such conditions has been illustrated for the 2009 L’Aquila earthquake.

We implemented this algorithm in I.D.L. (Interactive Data Language by ITT Visual Information Solutions) as a new module of the software for geodetic data inversion developed in recent years at the Remote Sensing Laboratory of INGV, in Rome. In the implementation particular attention was paid to the computation time and extra convergence criteria were included in order to avoid an overflow of patches. Our implementation is available, on demand, for distribution to the scientific community. It is integrated within our general inversion software and uses specific standards and

file formats (mostly ESRI shapefiles), but can easily be adapted to different languages and platforms.

## **8. ACKNOWLEDGMENTS**

We thank the anonymous reviewers for the suggestions that greatly contributed to improve this work; Stephen Monna for the long discussions on the data error and matrix resolution, John McCloskey and Rachel Cassidy who reviewed the English. This work is partially funded by the Italian Space Agency (ASI) through the SiGRiS project.

## **9. REFERENCES**

Anzidei, M., Boschi, E., Cannelli, V., Devoti, R., Esposito A., Galvani, A., Melini, D., Pietrantonio, Riguzzi, F., Sepe, V. & Serpelloni, E., 2009. Coseismic deformation of the destructive April 6, 2009 L'Aquila earthquake (central Italy) from GPS data, *Geoph. Res. Lett.*, 36, 117307, doi: 10.1029/2009GL039145, 2009.

Atzori, S., Hunstad, I., Chini, M., Salvi, S., Tolomei, C., Bignami, C., Stramondo, S., Trasatti, E. Antonioli, A. & Boschi, E., 2009. Finite fault inversion of DInSAR coseismic displacement of the 2009 L'Aquila earthquake (Central Italy), *Geoph. Res. Lett.*, 36, 115305, doi: 10.1029/2009GL039293

Biggs, J., Bergman, E., Emmerson, B., Funning, G., Jackson, J., Parsons, B. & Wright, T.J., 2006. Fault identification for buried strike-slip earthquakes using InSAR: The 1994 and 2004 Al Hoceima, Morocco earthquakes, *Geophys. J. Int.*, 166, 1347-1362, doi: 10.1111/j.1365-246X.2006.03071.x

Blewitt, G., Y. Bock & Kouba, J., 1994. Constraining the IGS Polyhedron by Distributed Processing, workshop proceedings: *Densification of ITRF through Regional GPS Networks*, held at JPL, Nov30-Dec 2, 1994, pp. 21-37.

Cheloni, D., D'Agostino, N., D'Anastasio, E., Avallone, A., Mantenuto, S., Giuliani, R., Mattone, M., Calcaterra, S., Gambino, P., Dominici, D., Radicioni, F. & Fastellini, G., 2010. Coseismic and initial post-seismic slip of the 2009Mw 6.3 L'Aquila earthquake, Italy, from GPS measurements, *Geophys. J. Int.*, 181, 1539-1546, doi: 10.1111/j.1365-246X.2010.04584.x.

Chiarabba, C., Amato, A., Anselmi, M., Baccheschi, P., Bianchi, I., Cattaneo, M., Cecere, G., Chiaraluce, L., Ciaccio, M.G., De Gori, P., De Luca, G., Di Bona, M., Di Stefano, R., Faenza, L., Govoni, A., Improta, L., Lucente, F.P., Marchetti, A., Margheriti, L., Mele, F., Michelini, A., Monachesi, G., Moretti, M., Pastori, M., Piana Agostinetti, N., Piccinini, D., Roselli, P., Seccia, D. & Valoroso, L., 2009. The 2009 L'Aquila (central Italy) Mw6.3 earthquake: Main shock and aftershocks, *Geoph. Res. Lett.*, 36,L18308, doi:10.1029/ 2009GL039627

Cirella, A., Piatanesi, A., Cocco, M., Tinti, E., Scognamiglio, L., Michelini, A., Lomax, A. & Boschi, E., 2009. Rupture history of the 2009 L'Aquila (Italy) earthquake from non-linear joint inversion of strong motion and GPS data, *Geoph. Res. Lett.*, 36, L19304, doi:10.1029/2009GL039795

Custodio, S., Page, M. T. & Archuleta, R.J., 2009. Constraining earthquake source inversions with GPS data: 2. A two-step approach to combine seismic and geodetic data sets, *J. Geoph. Res.*, 114, B01315, doi:10.1029/2008JB005746.

Fialko, Y., Sandwell, D., Simons, M. & Rosen, P, 2005. Three-dimensional deformation caused by the Bam, Iran, earthquake and the origin of shallow slip deficit, *Nature*, 435, 295-299, doi:10.1038/nature03425.

Franceschetti, G & Lanari, R., 1999. *Synthetic Aperture Radar Processing*, CRC Press Inc, Boca Raton, Florida.

Fukahata, Y. & Matsu'ura, M., 2005. General expressions for internal deformation fields due to a dislocation source in a multilayered elastic half-space, *Geophys. J. Int.*, 161, doi: 10.1111/j.1365-246X.2005.02594.x

Funning, G.J., Parsons, B. & Wriqth, T.J., 2005. Surface displacements and source parameters of the 2003 Bam (Iran) earthquake from Envisat advanced synthetic aperture radar imagery, *J. Geophys. Res.*, 110, B09406, doi:10.1029/2004JB003338.

Gabriel A.K, Goldstein, R.M & Zebker, H.A., 1989. Mapping Small Elevation Changes Over Large Areas: Differential Radar Interferometry, *J. Gheopys. Res.*, 94(B7), 9183-9191.

Hanssen, R., 2001. *Radar Interferometry: Data Interpretation and Error Analysis*, Remote Sens. Digital Image Process., vol. 2, Kluwer Acad., Dordrecht, Netherlands.

Johnson, K.M., Hsu, Y.J., Segall, P. & Yu, S.B., 2001. Fault geometry and slip distribution of the 1999 Chi-Chi, Taiwan earthquake imaged from inversion of GPS data, *Geoph. Res. Lett.*, **28**(11), 2285-2288.

Jónsson, S., Zebker, H.A., Segall, P. & Amelung, F., 2002. Fault slip distribution of the 1999 Mw7.2 HectorMine earthquake, California, estimated from satellite radar and GPS measurements, *Bull. seism. Soc. Am.*, 92, 1377–1389.

Lohman, R. & Simons, M., 2005. Some thoughts on the use of InSAR data to constrain models of surface deformation: Noise structure and data downsampling, *Geochem. Geophys. Geosyst.*, 6, Q01007, doi:10.1029/2004GC000841.

Massonnet, D., Rossi, M., Carmona, C., Adragna, F., Peltzer, G., Feigl, K. & Rabaute, T., 1993. The displacement field of the Landers earthquake mapped by radar interferometry, *Nature*, 364, 138– 142.

Menke, W., 1989. *Geophysical Data Analysis: Discrete Inverse Theory*, Academic Press (San Diego).

Okada, Y., 1985. Surface deformation due to shear and tensile faults in a half-space, *Bull. Seismol. Soc. Am.*, 75(4), 1135-1154.

Page, M.T., Custódio, S., Archuleta, R.J. & Carlson, J.M., 2009. Constraining earthquake source inversions with GPS data: 1. Resolution-based removal of artifacts, *J. Geophys. Res.*, 114, B01314, doi:10.1029/2007JB005449.

Penrose, R.A., 1955. A generalized inverse for matrices, *Proc. Cambridge Phil. Soc.*, 51, 406-413.

Pritchard, M.E., Simons, M., Rosen, P., Hensley, S. & Webb, F.H., 2002. Co-seismic slip from the 1995 July 30  $M_w=8.1$  Antofagasta, Chile, earthquake as constrained by InSAR and GPS observations, *Geophys. J. Int.*, 150, 362-376.

Reilinger, R.E., Ergintav, S., Bürgmann, R., McClusky, S., Lenk, O., Barka, A., Gurkan, O., Hearn, L., Feigl, K. L., Cakmak, R., Aktug, B., Ozener, H. & Töksoz, M.N., 2000. Coseismic and postseismic fault slip for the 17 August 1999,  $M=7.5$ , Izmit, Turkey Earthquake, *Science*, 289, 1519-1524.

Sagiya, T. & Thatcher, W., 1999. Coseismic slip resolution along a plate boundary megathrust: The Nankai Trough, southwest Japan, *J. Geoph. Res.*, 104(B1), 1111-1129

Simons, M., Fialko, Y & Rivera, L., 2002. Coseismic Deformation from the 1999  $M_w$  7.1 Hector Mine, California, Earthquake as Inferred from InSAR and GPS Observations, *Bull. Seismol. Soc. Am.*, 92(4), 1390-1402.

Stramondo, S., Chini, M., Bignami, C., Salvi, S & Atzori, S, 2011. X-, C-, and L-Band DInSAR Investigation of the April 6, 2009, Abruzzi Earthquake, *IEEE Geosci. Rem. Sens. Lett.*, 8(1), doi:10.1109/LGRS.2010.2051015

Sudhaus, H. & Jónsson, S., 2008. Improved source modelling through combined use of InSAR and GPS under consideration of correlated data errors: application to the June 2000 Kleifarvatn earthquake, Iceland, *Geophys. J. Int.*, 176, 389-404, doi: 10.1111/j.1365-246X.2008.03989.x.

Trasatti, E., Giunchi, C. & Piana Agostinetti, N., 2007. Numerical inversion of deformation caused by pressure sources: application to Mount Etna (Italy), *Geoph. J. Int.*, , doi: 10.1111/j.1365-246X.2007.03677.x

Wang, R., Martin, F.L. & Roth, F., 2003. Computation of deformation induced by earthquakes in a multi-layered elastic crust—FORTRAN programs EDGRN/EDCMP, *Comp. and Geosci.*, 29(2), 2003.

Wright, T.J., Lu, Z. & Wicks, C., 2003. Source model for the Mw 6.7, 23 October 2002, Nenana Mountain Earthquake (Alaska) from InSAR, *Geophys. Res. Lett.*, 30(18), 1974, doi:10.1029/2003GL018014.

10. FIGURES

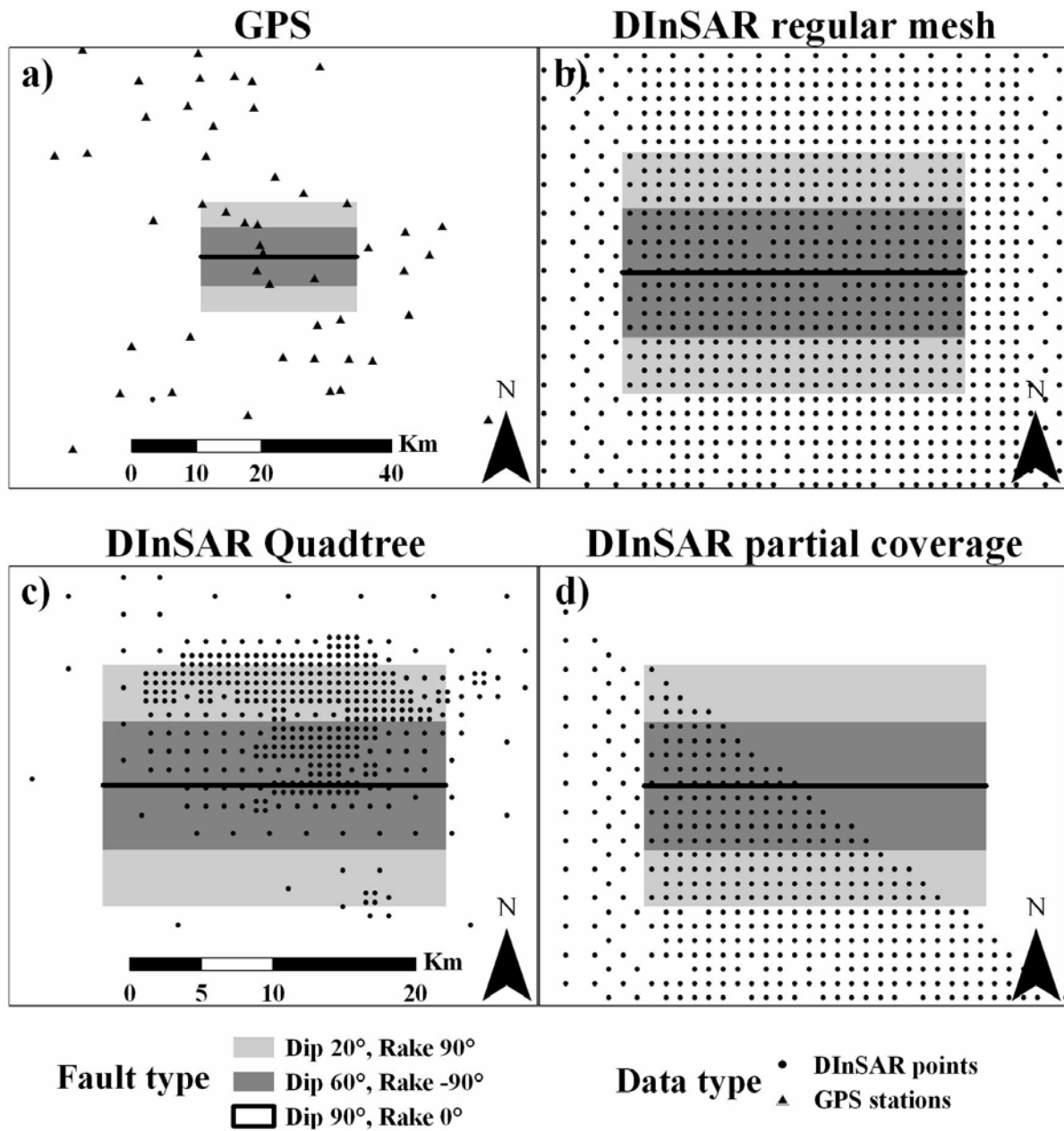


**Fig 1.** Map view of the data distribution used for the test: (a) sparse GPS measurements; (b) regularly sampled DInSAR data; (c) DInSAR data subsampled with Quadtree algorithm; (d) DInSAR data with partial coverage of the fault. The location of the three faults adopted is also shown: light gray for thrust fault (dip 20°, rake 90°), dark gray for normal fault (dip 60°, rake -90°) and a black line for the trace of transcurrent fault (dip 90°, rake 0°).

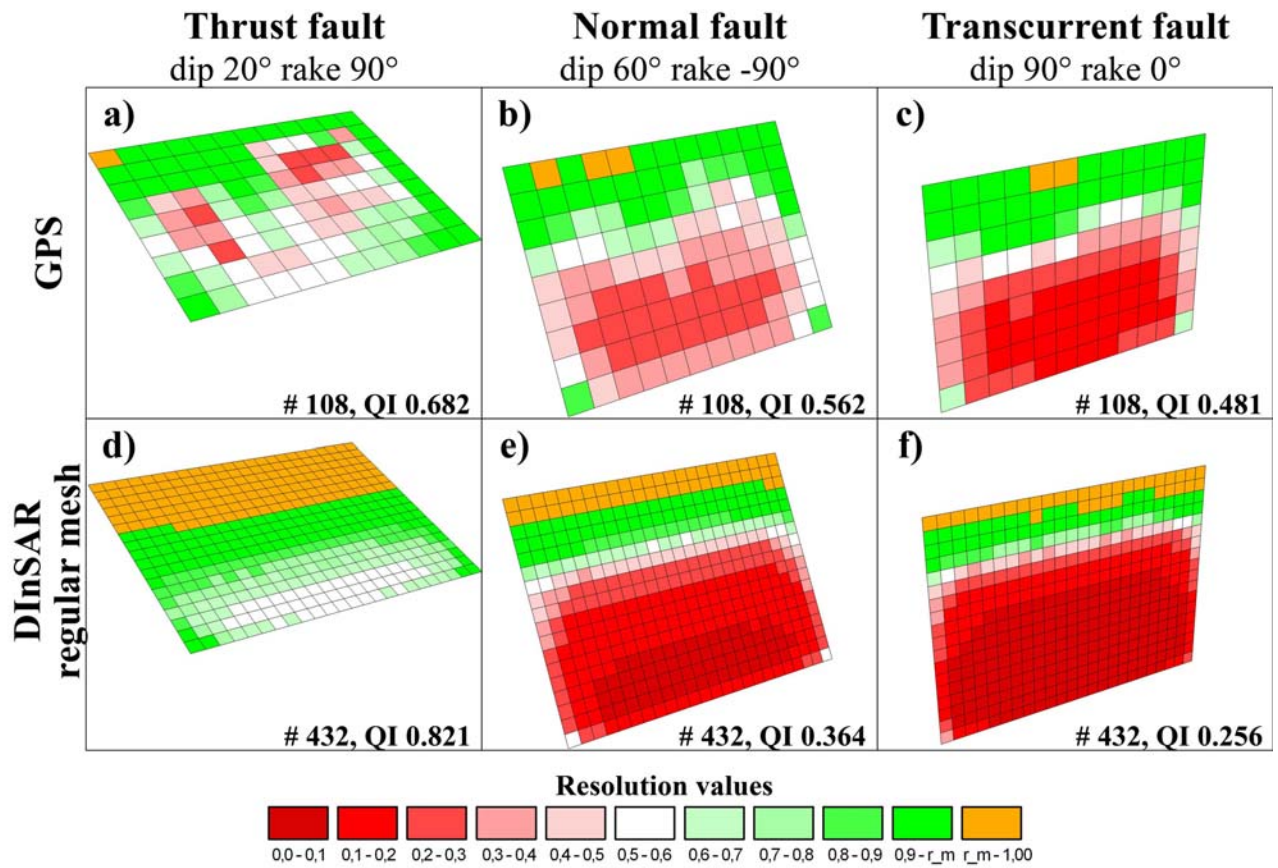


**Fig. 2.** Resolution values for a fault divided into patches of 2x2 km for GPS (a, b, c) and 1x1 km for DInSAR (d, e, f). a) and d) refer to a thrust fault (dip 20°, rake 90°); b) and e) to a normal fault (dip 60°, rake -90°); c) and f) refers to a strike slip fault (dip 90°, rake 0°), as in Fig. 1. Colors reflect the resolution value: the resolution power in red areas is overestimated while yellow patches are perfectly resolved and could be further subdivided (the resolution power is underestimated). The green patches are correctly sized. In the legends,  $r_m$  stands for  $res\_max$  (see Section 3)

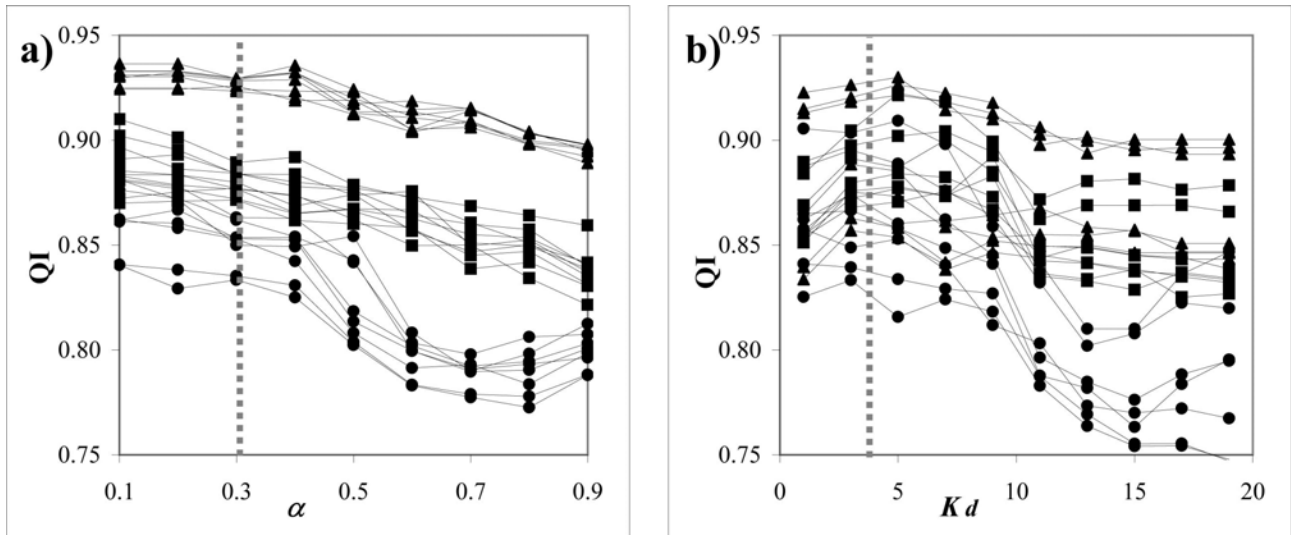


**Fig. 3** Effect of the parameters  $\alpha$  and  $k_d$  on the Quality Index (QI). In a) QI is a function of the percentage  $\alpha$ : the higher the value of  $\alpha$ , the lower the quality of the result and the computation time: very low  $\alpha$  values dramatically lower the computing performance without a significant improvement. b) QI as function of  $k_d$ : as the exponential factor  $k_d$ , increases the deepest parts of the fault are increasingly penalized. Dotted gray lines define the default values: 0.3 for  $\alpha$  and 3.5 for  $k_d$ . Square symbols refer to normal mechanisms ( $45^\circ < \text{dip} < 60^\circ$ ;  $-100^\circ < \text{rake} < -80^\circ$ ), circles to thrust faults ( $20^\circ < \text{dip} < 35^\circ$ ;  $80^\circ < \text{rake} < 100^\circ$ ), triangles to transcurrent faults ( $\text{dip} = 90^\circ$ ,  $-10^\circ < \text{rake} < 10^\circ$ ). In the tests, dip and rake values are randomly chosen between the given limits.

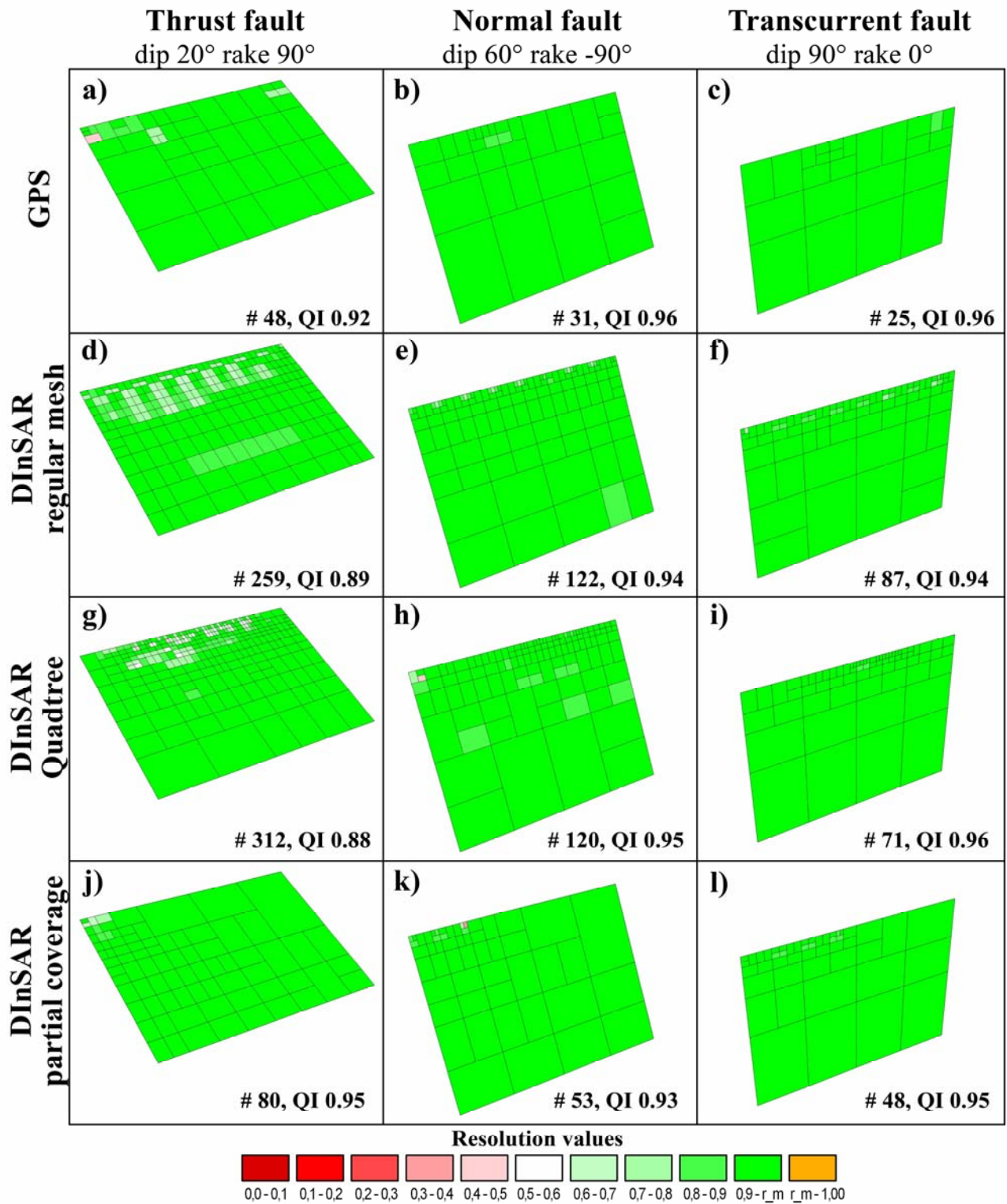


**Fig. 4.** Examples of fault subdivision for the geometries and mechanisms of Fig. 2 and the data distributions of Fig. 1. For each configuration we point out the number of patches and the Quality Index (QI).

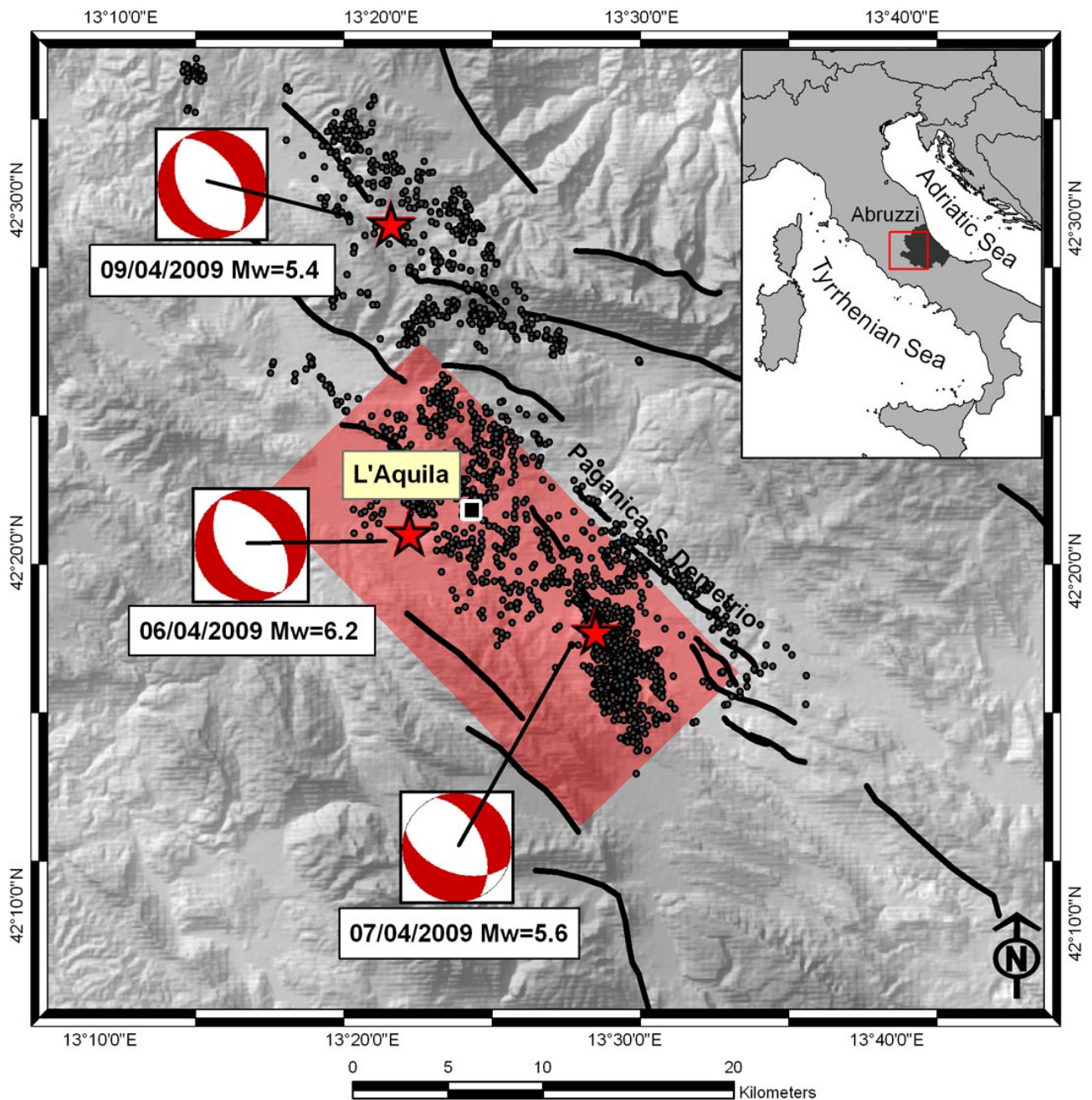


**Fig. 5.** Area of interest for the 2009 seismic sequence. Focal mechanisms for the  $M_w$  6.2 mainshock and the two earlier  $M_w > 5.0$  aftershocks are shown. Small circles are the relocated aftershocks until June 26, 2009 from *Chiarabba et al.* (2009). The Paganica – S. Demetrio fault, which was responsible for the main event, is indicated along with the other geologically mapped active faults in the region. The red rectangle defines the planimetric boundaries of the fault surface used in the linear inversion.

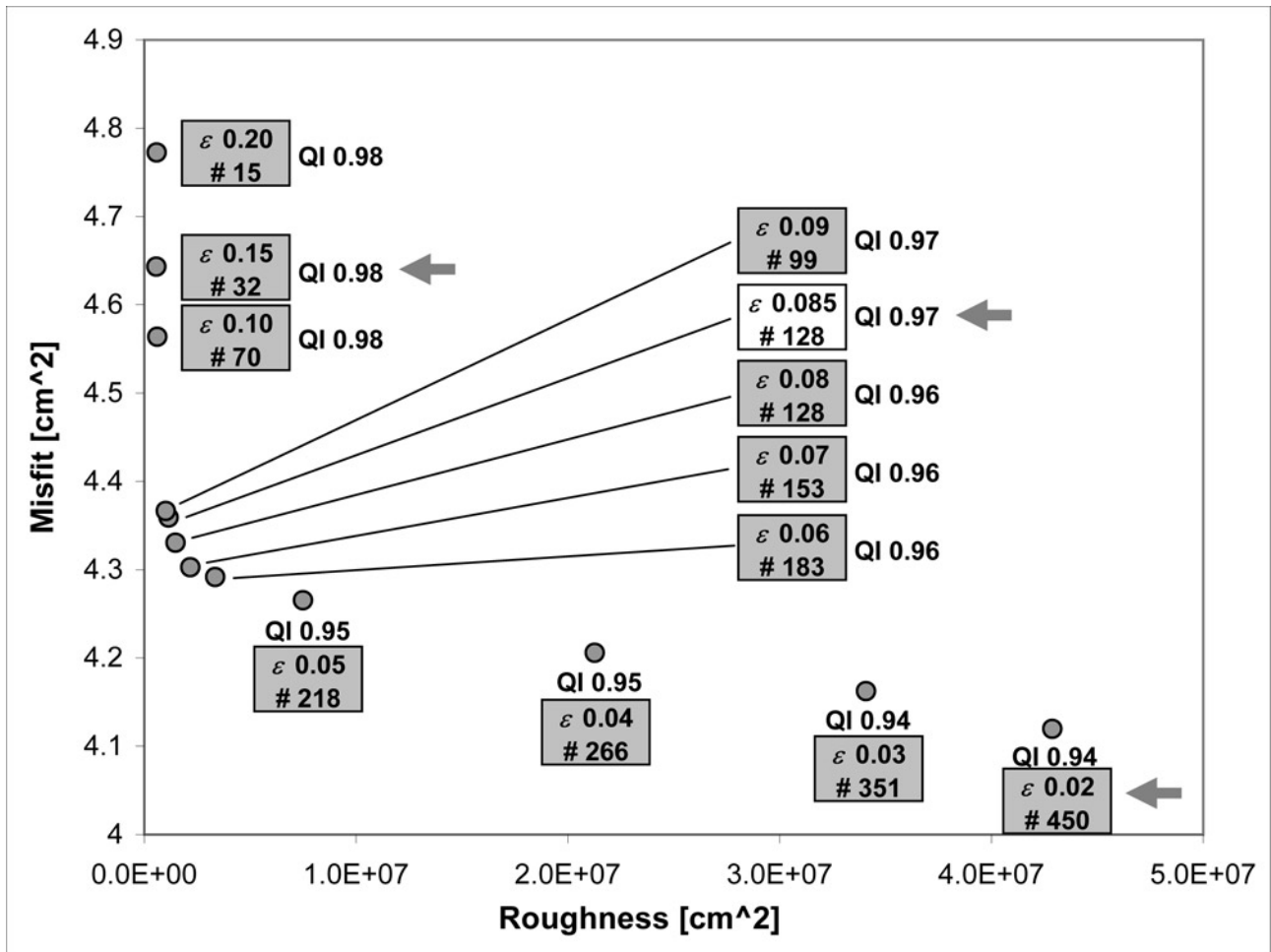


**Fig 6.** Trade-off between data fit and roughness for several values of the damping factor  $\varepsilon$ . The boxes show the damping factor and the corresponding number of patches, together with the Quality Index; the best solution is delineated in white. For the three solutions indicated by the gray arrows we show the slip distribution and the resolution values in Fig. 7.

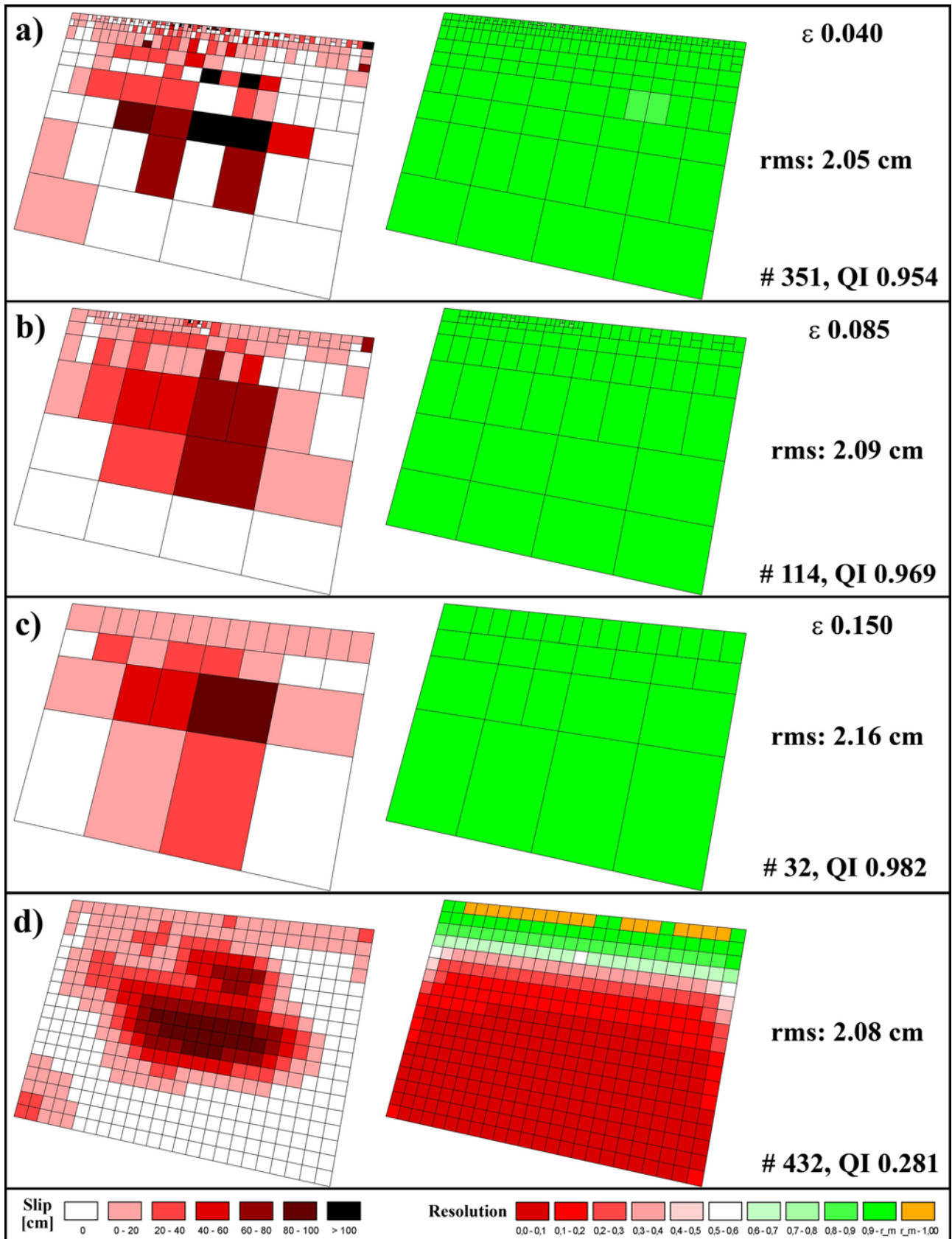


**Fig. 7.** Slip distribution, left, and resolution values, right, with a) a low level of damping ( $\varepsilon=0.04$ ), b) a correct damping ( $\varepsilon=0.085$ ) and c) excessive damping ( $\varepsilon=0.15$ ). For each solution we report the

damping value, the number of patches, the Quality Index (QI) and the rms of the residuals between the observed and the modeled data; d) is the solution with a fault divided in regular patches of 1 km x 1 km, retrieved with the linear inversion technique described in *Atzori et al. (2009)*.